ADVANCED ENGINEERING MATERIALS
www.aem-journal.com

Influence of Heat Treatment on Microstructure and Mechanical Properties at Elevated Temperatures of Nonweldable Ni-Based Alloy Printed by Fused Filament Fabrication

Haneen Daoud, Ying Zheng, Agata Kulig, Natalja Agarkov, Esma Mese, Wolfgang Hofmann, Peter Würtele, and Uwe Glatzel*

The microstructure and mechanical properties of printed specimens of nonweldable MAR-M247 alloy in the sintered state and after different heat treatments are investigated. Specimens are produced using the fused filament fabrication process, which enables the fabrication of crack-free components. The microstructure is characterized by scanning electron microscopy, electron backscatter diffraction, and X-ray diffraction. Tensile tests are conducted at room temperature, 500, 600, and 700 °C. All heat-treated specimens exhibit the formation of γ′ (gamma prime) precipitates larger than 500 nm, along with various carbides and equiaxed grain structures. The as-heat-treated specimens at the high subsolvus temperature of 1220 °C show the highest tensile strength with the highest elongation and stable tensile strength up to 700 °C.

1. Introduction

Nonweldable and difficult-to-weld alloys exhibit superior properties in terms of hardness, wear, and thermomechanical properties and are of significant importance in many industrial applications.[1,2] Additive manufacturing (AM) technologies have attracted much attention in recent years due to their ability to produce more complex geometries in a resource-efficient manner.[3] Various materials have been successfully printed and used industrially, such as IN718,[4–9] Al-Si-Mg alloys,[10–13] and Ti-6Al-4 V alloy.[14–16] However, nonweldable and difficult-to-weld alloys suffer from a high susceptibility to cracking during AM processing.[1,2,17] These alloys have been produced by casting, for example, where slow solidification rates and low gradients predominate. Rapid solidification and high gradients prevail in laser-based AM processing. These solidification conditions permit high levels of residual stress in the printed components. This can lead to different types of cracking at different stages of processing and during solidification.[1,2,17] There is therefore a high demand to print crack-free and fully dense components of these materials using AM.

Several attempts have been initiated to produce crack-free and fully dense specimens from nonweldable alloys as high-strength low steels using laser-based AM processes.[18–21] J. J. S. Dilip et al. reported optimized process parameters to produce fully dense, crack-free specimens of low alloy steel HY100 using laser powder bed fusion PBF-LB/M.[19] The effect of preheating the build plate to 160 °C in the PBF-LB/M process to prevent cracking during printing of AISI 4130 has been reported by Xinwei Li et al.[20] Raiyan Seede et al. supported the process optimization of PBF-LB/M by applying analytical models to predict the melt pool geometry to simulate pore formation in low alloy martensitic steel, AF9628-printed specimen.[21]

Printing of nonweldable Ni-based alloys has also been attempted in recent years, mainly via PBF-LB/M and electron beam melting (PBF-EB/M) processes, due to the high creep resistance at elevated temperatures.[1,17,22–25] This superior performance is a result of the high volume fraction of γ′-precipitates. Weldability deteriorates significantly when the aluminum (Al) and titanium (Ti) content exceeds 4 wt% in Ni-based superalloys.[26,27] Alloy MAR-M247 is characterized by poor weldability due to its high Al and Ti content of 7 wt% and is mainly processed by conventional methods such as vacuum casting or metal injection molding (MIM).[28,29] This alloy exhibits high creep strength and good castability together with excellent resistance to oxidation and corrosion at elevated

H. Daoud, Y. Zheng, A. Kulig, N. Agarkov, E. Mese, U. Glatzel
Metal Division
Neue Materialien Bayreuth GmbH
Gottlieb-Keim-Strasse 60, 95448 Bayreuth, Germany
E-mail: haneen.daoud@nmbgmbh.de

W. Hofmann, P. Würtele
Peter Würtele GmbH
Industriestrasse 26, 97631 Bad Königshofen, Germany

U. Glatzel
Metals and Alloys
University of Bayreuth
Prof.-Rüdiger-Bormann-Str. 1, 95447 Bayreuth, Germany

The ORCID identification number(s) for the author(s) of this article can be found under https://doi.org/10.1002/adem.202500589.

DOI: 10.1002/adem.202500589

temperatures.[17,28–30] In the cast condition, the alloy has a high volume fraction (62% by volume) of γ′-precipitates [Ni_3(Al,Ti)]. M. Ramsperger et al. demonstrated the possibility of crack-free printing of alloy MAR-M247 by optimizing and controlling local process parameters during the PBF-EB/M process to stabilize a defined grain morphology and microstructure.[2] The influence of the laser scanning strategy on the grain structure and cracking behavior of printed Alloy MAR-M247 using PBF-LB/M was investigated by L. N. Carter et al.[24] The influence of high-temperature preheating up to 1200 °C during the PBF-EB/M process to suppress crack formation by reducing thermal gradients was investigated by Y.-C. Hagedorn et al.[31] A. Seidel et al. investigated the cracking behavior of alloy MAR-M247 during printing using powder-based laser melting deposition (DED-LB/M) with hybrid (laser and induction) heating sources.[32] The development of optimized, printable, nonweldable alloys based on computational materials modeling and big data has been explored to develop materials with similar properties at elevated temperatures.[33]

Laser-based AM processes in general are not only expensive to invest in, but also require a huge effort of trial and error, especially when printing nonweldable alloys. Therefore, sinter-based AM processes have recently been intensively investigated to produce crack-free components from nonweldable alloys.[9,34–36] This is due to the ability to print alloys at lower temperatures below 200 °C, as the metallic powders are mixed with polymeric binders. At these low temperatures there exists no thermal gradient and no cracking. However, a suitable range of parameters should be developed during sintering to avoid cracking. T. Dahmen et al. have successfully printed crack-free MAR-M247 specimens using binder jetting with similar room temperature (RT) tensile strength to specimens produced by conventional MIM or vacuum investment casting.[35] However, this was only possible by using hot isostatic pressing (HIP) to reduce porosity below 2%.[35,36] An additional HIP process in the sinter-based process chain not only increases the cost and processing time of printed parts, but also introduces additional critical process parameters that require precise control. This is particularly detrimental for nonweldable alloys, where cracking and thermal distortion are highly sensitive to the conditions of the post-processing steps.

Fused filament fabrication (FFF) offers an alternative manufacturing process for nonweldable alloys such as Alloy MAR-M247, as FFF is characterized by a lower investment cost compared to binder jetting. In this work, the FFF process without HIP is used to print crack-free specimens of the alloy MAR-M247. The main objective of this study is to investigate the influence of applying different heat treatments to the sintered specimens on the mechanical properties at elevated temperatures. For this purpose, highly filled MAR-M247 filament was used to print cubic and tensile test specimens.

Table 1. Chemical composition of Ni-based superalloy MAR-M247 in weight percentage.

	Ni	Cr	Al	Mo	W	Co	Nb	Fe	Hf	Ta	C
M247	bal.	8	5.5	0.7	10	10	0.01	0.2	1.3	3	0.16

2. Experimental Section

The powder used to manufacture the filament was the nonweldable nickel-based superalloy MAR-M247 (ECKART TLS GmbH, Bitterfeld Wolfen, Germany). The chemical composition is given in **Table 1**. The average particle size distribution was smaller than 32 µm. Highly filled metal filaments with a metal content of at least 92 wt% and an average diameter of 1.75 mm were manufactured by Peter Würtele GmbH.

All specimens were printed using an AM-Xfuse One FFF printer (AM Extrusion GmbH, Radebeul, Germany). The specimens were sliced using Cura 3D software (Ultimaker BV, Utrecht, The Netherlands). The dimensions of the printed specimens were $20 \times 10 \times 10\,mm^3$. For the tensile tests, flat specimens were prepared in the horizontal xy-direction (**Figure 1**). To achieve high density and minimal porosity, all specimens in this study were printed with a line pattern with a fill structure and a fill rate of 100%. In addition, all layers of the specimens were built up in the xy-direction and with a shell of four outlines (**Figure 2**). The optimization of the process parameters (printing and sintering) was carried out in an internal research project. For this study, only the optimized process parameters and printing strategies were considered (**Table 2**).

Printed specimens were solvent debinded in acetone (99.98%, Fisher Scientific) at 40 °C for 24 h and then dried at RT. This was followed by thermal debinding in a horizontal APM tube furnace operating under argon (GLO 8/13, Carbolite Gero, Germany). Finally, the brown specimens were sintered in a horizontal ceramic tube furnace (TF 16/100/450, Carbolite Gero,

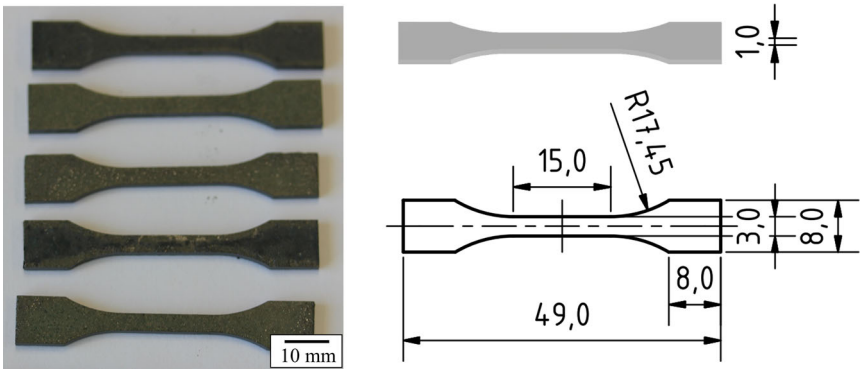

Figure 1. Tensile test specimens manufactured using the FFF process and their geometry. All dimensions are in [mm].

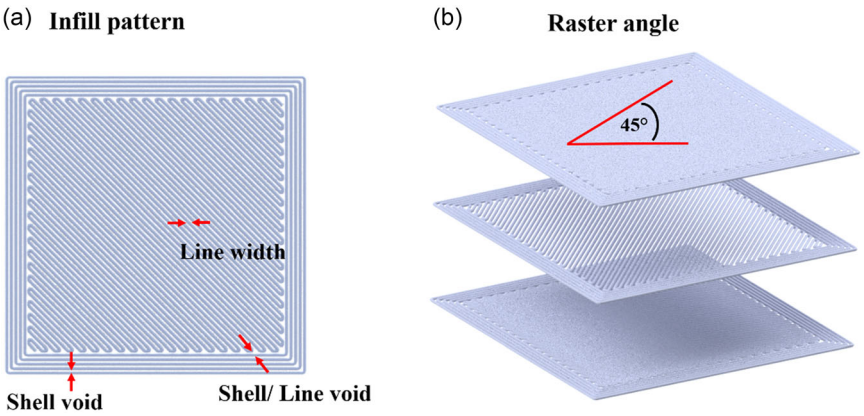

Figure 2. Applied printing strategy: a) single layer and b) multiple layers.

Table 2. Optimized printing parameters used for MAR-M247 alloy in this study.

Parameter	
Line width	0.40 mm
Layer height	0.12 mm
Infill speed	40 mm s^{-1}
Shell speed	20 mm s^{-1}
Nozzle temperature	115 °C
Bed temperature	RT
Flow rate	100%

Germany). The applied optimized sintering parameters are 1310 °C with a heating rate of 5 K min^{-1} under a vacuum atmosphere of 10^{-6} mbar for 12 h. Two different heat treatments were carried out on the as-sintered specimens (**Figure 3**). For this purpose, heat treatments 1 and 2 were conducted in a sintering furnace TF 16/100/450 (Carbolite Gero, Germany) and a laboratory furnace (KLS15/12, Thermconcept, Germany), respectively.

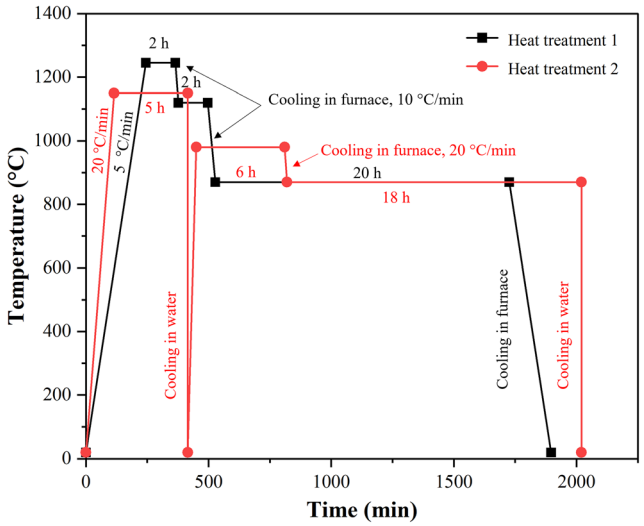

Figure 3. Heat treatments applied to the as-sintered specimens.

Cross-sections of the as-sintered, as-heat-treated specimens were mechanically grinded, polished, and etched, for the analysis of the microstructures with a scanning electron microscope, SEM (Zeiss EVO MA15, Germany) equipped with an energy dispersive X-ray spectrometer (EDX) and electron backscatter diffraction (EBSD). For EBSD analysis samples were further polished for 8 h using OP-U 0.08 µm colloidal silica suspension on Buehler's VibroMet 2 vibratory polishing machine (Esslingen, Germany). Grain size and volume fraction were quantified using the TSL OIM Data Collection system (AMETEK), based on orientation maps obtained from EBSD analysis. Phase identification was performed by X-ray diffraction, XRD (Bruker D8 advance diffractometer, Germany). ImageJ image analysis software was used to measure the porosity of the as-sintered specimens and the volume percentage of carbides and phases. Tensile tests were performed at RT on a Kammrath and Weiss micro-tensile-testing device (Kammrath and Weiss GmbH, Germany) using a strain rate of $\approx 1.3 \times 10^{-3}$ s^{-1}. Only the as-heat-treated 1 specimens were subjected to tensile tests at elevated temperatures of 500, 600, and 700 °C.

3. Results

3.1. Microstructure of Printed MAR-M247 Alloy

3.1.1. As-Sintered Specimens

The porosity of the as-sintered specimens varies from 4 to 9%. The pores are not homogeneously distributed. Mechanical tests were only performed on specimens with the lowest porosity. The shrinkage percentage is 8.9 ± 0.2%. The γ′-precipitates in the γ-matrix have a volume fraction of 20 ± 3.2% with a length of 200–500 nm (**Figure 4**a). The XRD diffraction pattern in **Figure 5** indicates the presence of γ/γ′ phases. The EBSD analysis shows the growth of equiaxed grains with a size of 17 ± 10 µm, with no preferred orientation.

3.1.2. As-Heat-Treated Specimens

The volume fraction of γ′-precipitates in the as-heat-treated 1 specimens is 50 ± 10% with varying lengths from 500 nm to 1.5 µm (Figure 4c,d). The XRD diffraction pattern in Figure 5

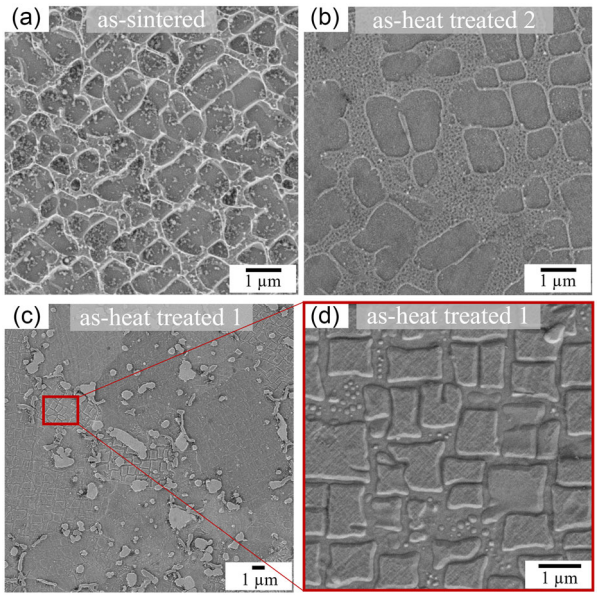

Figure 4. SEM micrographs of the specimens a) as-sintered, b) as-heat-treated 2, and c,d) as-heat-treated 1.

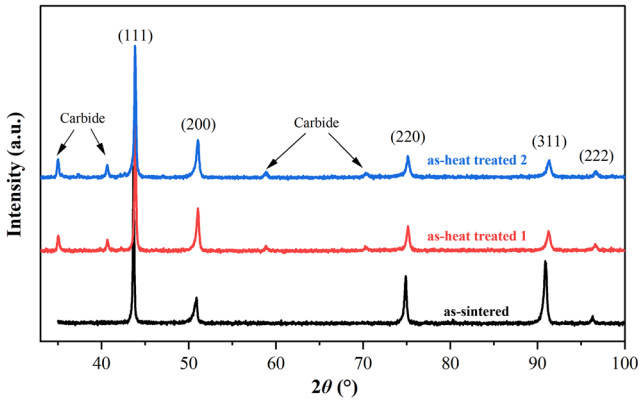

Figure 5. XRD diffraction patterns of the specimens investigated in as-sintered, as-heat-treated 1, and as-heat-treated 2 conditions.

shows peaks belonging to carbide formation in addition to γ/γ′ phases. The EBSD analysis reveals the growth of equiaxed grains with a size of 22 ± 11 μm, with no preferred orientation. Elemental analysis with energy-dispersive spectroscopy (EDS) mapping shows the formation of three different carbides: W-rich, Cr-rich, and Ta/Ti/Hf-rich. Large W-rich blocks with lengths varying from 0.5 μm to very large blocks with lengths up to several micrometers are located along the grain boundaries (**Figure 6**). Fine Cr-rich chains appear at the grain boundaries. While small block and round Ta/Ti/Hf-rich carbides are distributed within the grains and along the grain boundaries. The chemical composition of the carbides in the as-heat-treated 1 specimens is shown in **Table 3**. The percentage of large carbides is about 16 vol%.

The as-heat-treated 2 specimens have γ′-precipitates with a length of 500 nm–1 μm with a volume fraction of 23.7 ± 2.8%. Carbide peaks are visible in the XRD diffraction pattern (Figure 5). Equiaxed grains with a size of 7.1 ± 5.3 μm are stabilized, as shown in **Figure 7**. Similar carbides are found and analyzed as specimens under heat treatment conditions 1 (EDS analyses are not shown here). However, the sizes of the carbides formed are significantly smaller, with a low percentage of 3 vol%.

3.2. Tensile Properties of Printed MAR-M247 Alloy

3.2.1. Tensile Properties at RT

Figure 8a shows the tensile stress–strain curves of the as-heat-treaded 1 & 2 specimens at RT. The UTS and elongation for as-heat-treated 1 specimens are the highest compared to as-heat-treated 2 specimens at RT. The as-heat-treated 1 specimens have an UTS of 683 ± 27 MPa and an elongation of 10 ± 0.5%. In

Table 3. Chemical composition of the carbides in the as-heat-treated 1 specimens (at%), standard deviation less than 2.5%.

Carbides	C	Al	Ti	Cr	Co	Ni	Hf	Mo	Ta	W
Ta, Hf-rich	59.89	2.64	6.20	1.82	1.27	15.19	2.70	–	5.94	2.57
Cr-rich	47.62	–	–	10.62	3.00	13.98	–	–	–	19.4
W-rich	49.49	0.59	0.84	8.61	1.37	14.21	–	0.57	–	15.27

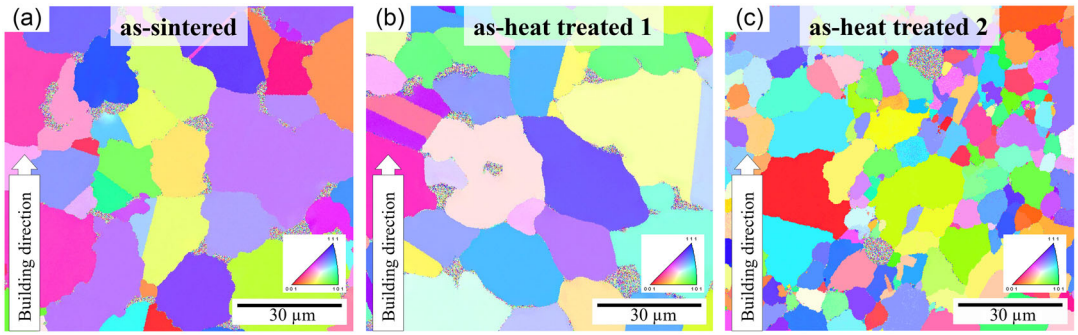

Figure 6. EBSD-images of the microstructure for a) as-sintered, b) as-heat-treated 1, and c) as-heat-treated 2 specimens. The grain orientation is indicated in building direction.

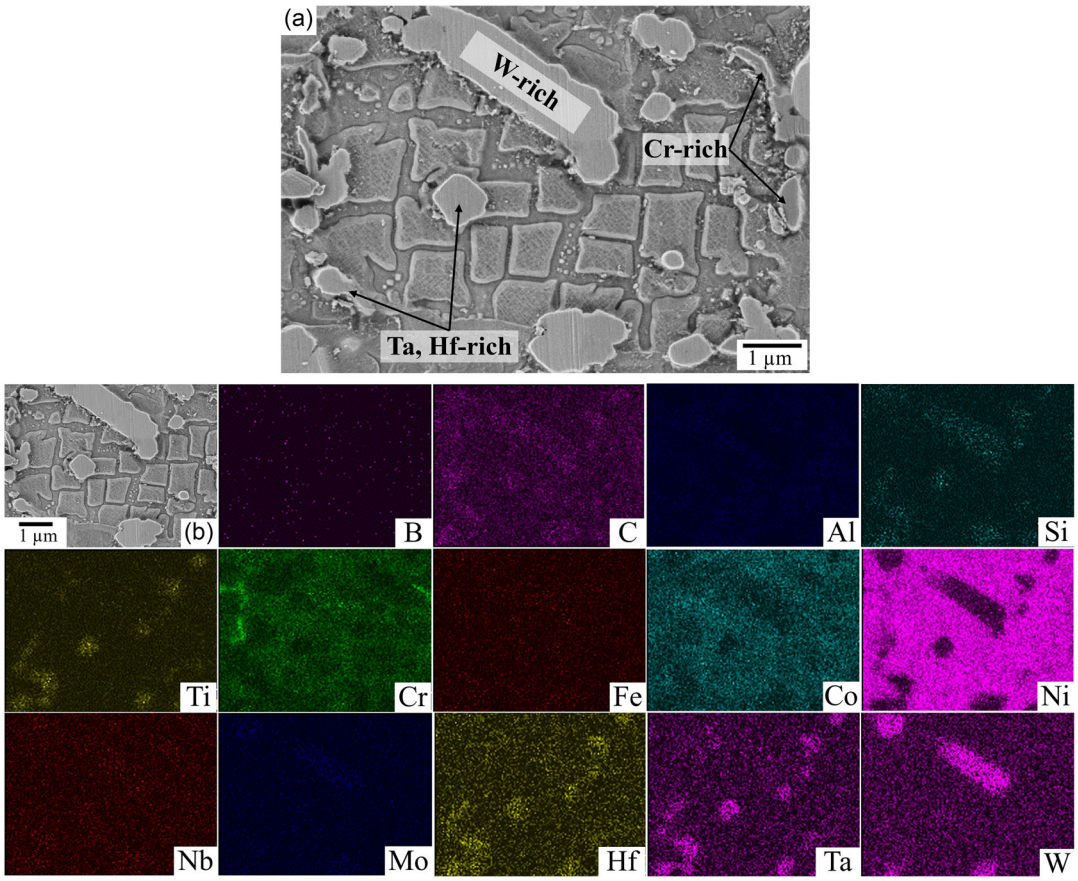

Figure 7. Energy-dispersive spectroscopy (EDX) elemental mapping results of formed three different carbides formed in the as-heat-treated specimen 1.

contrast, after heat treating condition 2, a slightly lower UTS of 604 ± 53 MPa can be achieved with a significantly lower elongation of $4 \pm 0.4\%$.

3.2.2. Tensile Properties at Elevated Temperatures

Only as-heat-treated 1 specimens were tested for tensile strength at 500, 600, and 700 °C. Figure 8b shows the resulting tensile stress–strain curves. Both UTS and elongation values were in the same range at the temperatures tested. The UTS values are 723 ± 59, 722 ± 53, and 709 ± 32 MPa at 500, 600, and 700 °C, respectively. Whereas, the elongation values are $10 \pm 4\%$, $9.3 \pm 2\%$, and $9.6 \pm 0.5\%$ at 500, 600, and 700 °C, respectively.

4. Discussion

4.1. Effect of Heat Treatment on the Microstructure of As-Sintered Specimens

The mechanical properties of alloy MAR-M247 are highly dependent on the γ' sizes, carbide morphology, and their volume fractions. These are controlled by the heat treatment process. Typically, the heat treatment routes for the as-cast specimens consist of a supersolvus solution heat treatment (SH; <1240 °C) followed by two-step aging. The holding times and cooling rates are very essential to stabilize the phases.[2,28]

The main difference between heat treatment conditions 1 and 2 is the temperature of the solution treatment and the subsequent cooling rates. The as-heat-treated 1 specimens were heated to a higher solution temperature of 1220 °C followed by slow cooling in the furnace. Whereas, the as-heat-treated 2 specimens were set to 1180 °C followed by water quenching. The higher SH allowed a more homogeneous heat and phase distribution. The subsolvus SH generally permits partial dissolution of smaller γ'-precipitates and coarsening of larger precipitates, compared to the as-sintered specimens (see Figure 4a–d). The coarsening of the γ'-precipitates is significantly higher in the as-heat-treated 1 specimens than in the as-heat-treated 2 specimens as a result of the higher applied SH temperature (see **Figure 9**a). The in-furnace cooling allows the precipitation of carbides and the coarsening of grain sizes. In contrast, the SH followed by water quenching stabilizes the formation of fine precipitates and smaller grain sizes, as shown in Figure 4 and 7. The grain sizes of the as-heat-treated 1 specimens are the highest and those of the specimens as-heat-treated 2 are the lowest (see Figure 9b). The first aging step at 1160 °C in the as-heat-treated 1 conditions allows the precipitation of different large with higher volume fraction of carbides. All three types of carbides formed, Cr-rich

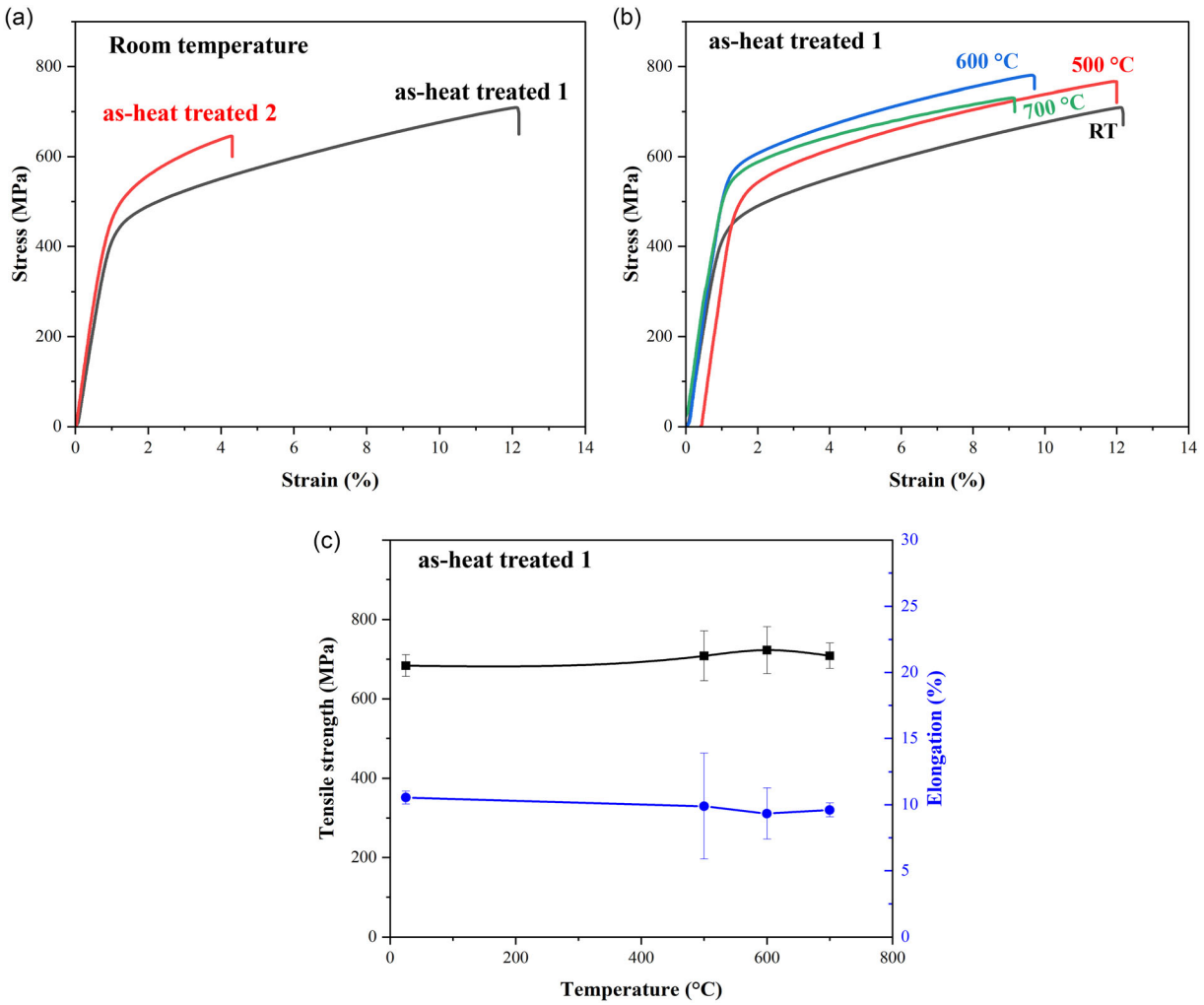

Figure 8. Tensile stress–strain curves for a) as-heat-treated specimens 1 and 2 at RT and b) at 500, 600, and 700 °C of as-heat-treated specimens 1; c) tensile strength and elongation as a function of temperature for as-heat-treated specimens 1.

chains as well as W- and Ta-rich precipitates, are coarser, for example, the length of the W-rich carbides at the grain boundaries exceeds several micrometers and they are the largest carbides compared to the Cr-rich chains and Ta-rich block precipitates (see Figure 4c and 6). In the case of as-heat-treated 2 specimens obviously finer and lower volume fraction of about 4%, are observed, see Figure 9c.

4.2. Effect of the Microstructure on the Tensile Properties

The UTS and elongation of the as-heat-treated 1 specimens at RT are higher than those of the as-heat-treated 2 specimens. This could be attributed to the higher volume fraction of γ′-precipitates and carbides as well as the effect of larger grain sizes, as summarized in Figure 9a–c. The tensile properties are highly dependent on the nature, size, and density of the different precipitates and carbides formed. The primary strengthening mechanisms in this alloy are precipitation strengthening and carbide formation, promoted by alloying elements such as Hf, Ta, W, and Cr. Both types of precipitates act as obstacles to dislocation motion.[29,37–39] The higher UTS observed for Heat Treatment 1 compared to Heat Treatment 2 is primarily due to the higher volume fraction of γ′ precipitates—≈50% compared to around 25%—as well as the formation of carbides, as shown in Figure 9. Furthermore, larger precipitates offer greater resistance to dislocation movement, requiring increased applied stress to initiate and sustain plastic deformation, thereby enhancing the material's strength and elongation.[29,37–39] **Figure 10** shows the fracture surfaces of the as-heat-treated specimens 1 and 2 after tensile testing at room temperature. The thinner gauge section of as-heat treated specimen 1, along with the higher density of dimples on the fracture surface, indicates a significantly higher elongation compared to as-heat-treated specimen 2. These observations are in good agreement with the measured results presented in Figure 8a.

At elevated temperatures up to 700 °C, stable mechanical properties are observed for the as-heat-treated 1 specimens. Both tensile strength and elongation remain in the same range. This behavior is known for various Ni-based superalloys as a result of

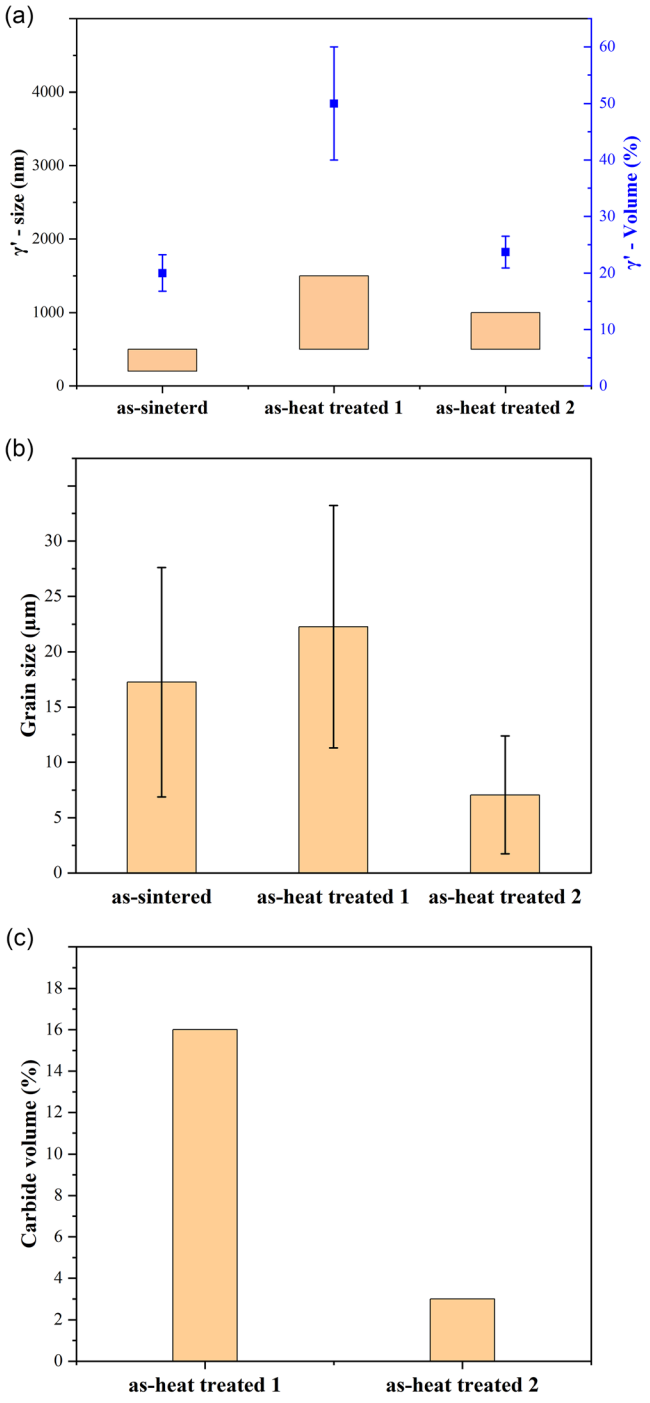

Figure 9. a) Gamma prime precipitate size and volume fraction, b) grain size, and c) carbide volume fraction for the as-sintered, as-heat-treated 1, and as-heat-treated 2 specimens.

formation stable γ′-precipitates in desired from and sizes and fractions.[2,28,37–41]

Figure 11 shows a comparison of tensile strength as a function of temperature between the printed MAR-M247 specimens produced with PBF-EB/M,[2] binder jetting (BJ),[34] and the as-heat-treated 1 specimens from this study. The highest UTS

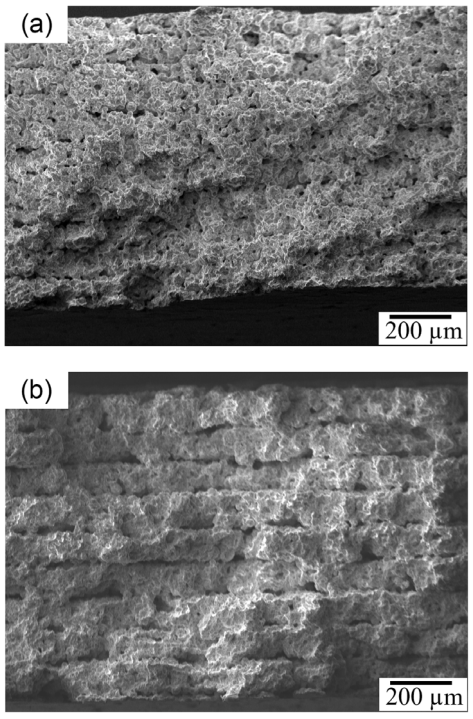

Figure 10. SEM image of the fracture surfaces after tensile testing at room temperature for: a) as-heat-treated specimen 1 and b) as-heat-treated specimen 2.

as a function of temperature is for the PBF-EB/M printed specimens and the lowest is for the printed specimens in this study. For the specimens cited above, the grains show equiaxed growth. For the BJ specimens, the grain sizes are in the range of 15–20 µm, which is in the same range as the specimens examined in this study. The γ′-precipitates in the PBF-EB/M specimens are very fine and homogeneous with a length of 0.4–0.5 µm. In the case of the BJ specimens, gamma prime precipitates with varying lengths of 0.5–1 µm are reported. The higher tensile strength of the PBF-EB/M specimens could be attributed to the very homogeneous formation and distribution of the γ′-precipitates. The fine distribution of gamma prime precipitates in parts produced by the PBF-EB/M process is primarily attributed to the intense thermal conditions during the build. In this process, the metal powders are fully melted by the electron beam, leading to a high degree of homogenization and rapid solidification. These conditions promote the uniform dispersion of gamma prime precipitates and can influence their morphology and distribution favorably.[3] In contrast, both BJ and FFF involve sintering of powder-based green parts, where only limited melting or solid-state diffusion occurs. As a result, the homogenization is less effective, and the distribution of gamma prime precipitates tends to be coarser and less uniform.

An important factor here is the residual porosity compared to the specimens used in this study. Both Ramsperger et al. and Martin et al. applied not only heat treatment steps but also the HIP process to densify the specimens. The PBF-EB/M specimens have the lowest porosity of less than 2% and therefore the highest mechanical properties. The BJ and PBF-EB/M

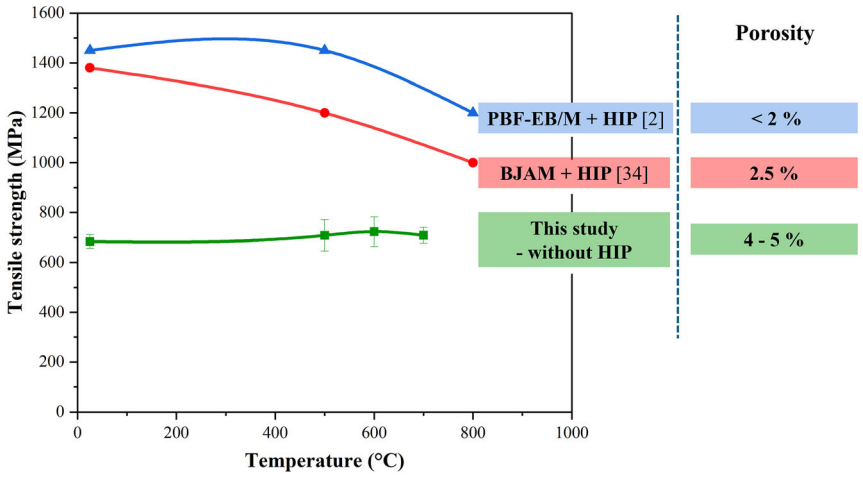

Figure 11. Comparison of tensile strength as a function of temperature between printed MAR-M247 specimens produced by PBF-EB/M and BJ and as-heat-treated 1 specimens from this study.

specimens show a marked decrease in tensile strength from 500 to 800 °C. The as-heat treated specimens show a more stable trend up to 700 °C. This could be attributed to the higher volume fraction and the type of the different carbides. However, the role of the different types of carbides (Cr-rich, W-rich, and Ta-rich) in stabilizing mechanical properties should be investigated in more detail.

5. Conclusion

Printed MAR-M247 alloy using FFF under as-sintered conditions and after heat treatment without HIP at room and elevated temperatures were investigated. Crack-free specimens of MAR-M247 alloy with a porosity of about 4% were successfully produced. The shrinkage percentage obtained after sintering the FFF-printed specimens is $8.9 \pm 0.2\%$.

At a high solution treatment temperature of 1220 °C, followed by slow cooling in the furnace, coarser γ′-precipitates with a volume fraction of 50% and varying lengths from 500 nm to 1.5 µm are observed. Three different types of coarse carbides, Cr-rich chain, W-rich blocks, and Ta-rich blocks are formed with volume fraction of 15%. The lower high solution treatment temperature of 1180 °C followed by rapid cooling in water initiates the formation of smaller γ′-precipitates with a length of 500 nm–1 µm with a volume fraction of 24%. This promotes the formation of fine carbides with a lower volume fraction of 4%.

The as-heat-treated 1 specimens have higher tensile strength and elongation than the as-heat-treated 2 specimens. The tensile strength at RT of the as-heat-treated 1 specimens is 683 ± 27 MPa and the elongation is $10 \pm 0.5\%$. The tensile properties remain stable at elevated temperatures up to 700 °C, where the tensile strength is maintained in the range of 700 MPa with an elongation of about 9.5%.

Acknowledgements

The authors thank the Federal Ministry for Economic Affairs and Climate Action for funding the FDM-MAR research project under grant number KK5027501 within the "Central Innovation Programme for small and medium-sized enterprises (SMEs)". Further thanks are given to all my colleagues and project partner for their supports.

Open Access funding enabled and organized by Projekt DEAL.

Conflict of Interest

The authors declare no conflict of interest.

Author Contributions

Haneen Daoud: conceptualization (lead); formal analysis (lead); funding acquisition (lead); investigation (lead); methodology (lead); project administration (lead); resources (lead); validation (lead); visualization (lead); writing—original draft (lead). **Ying Zheng**: conceptualization (equal); formal analysis (lead); investigation (lead); validation (equal); writing—review & editing (supporting). **Agata Kulig**: data curation (supporting); formal analysis (supporting); visualization (supporting). **Natalja Agarkov**: data curation (equal); formal analysis (equal); investigation (equal); validation (supporting); visualization (supporting). **Esma Mese**: conceptualization (supporting); data curation (supporting); formal analysis (equal); investigation (equal); validation (supporting); visualization (supporting). **Wolfgang Hofmann**: data curation (supporting); investigation (lead); methodology (equal); validation (supporting). **Peter Würtele**: data curation (supporting); investigation (equal); validation (supporting). **Uwe Glatzel**: funding acquisition (supporting); resources (supporting); supervision (supporting).

Data Availability Statement

The data that support the findings of this study are available on request from the corresponding author. The data are not publicly available due to privacy or ethical restrictions.

Keywords

additive manufacturing, fused filament fabrication, heat treatments, MAR-M247 alloys, nonweldable alloys, sintering

Received: February 28, 2025
Revised: May 14, 2025
Published online: June 10, 2025

[1] E. Chauvet, P. Kontis, E. A. Jägle, B. Gault, D. Raabe, C. Tassin, J.-J. Blandin, R. Dendievel, B. Vayre, S. Abed, G. Martin, *Acta Mater.* **2018**, *142*, 82.
[2] M. Ramsperger, S. Eichler, *Metall. Mater. Trans.* **2023**, *54*, 1730.
[3] C. Körner, *Int. Mater. Rev.* **2016**, *61*, 361.
[4] K. N. Amato, S. M. Gaytan, L. E. Murr, E. Martinez, P. W. Shindo, J. Hernandez, S. Collins, F. Medina, *Acta Mater.* **2012**, *60*, 2229.
[5] J. Strößner, M. T. U. Glatzel, *Adv. Eng. Mater.* **2015**, *17*, 1099.
[6] H. Helmer, C. Körner, R. Singer, *J. Mater. Res.* **2014**, *29*, 1987.
[7] A. Strondl, M. Palm, J. Gnauk, G. Frommeyer, *Mater. Sci. Technol.* **2011**, *27*, 876.
[8] Z. Wang, K. Guan, M. Gao, X. Li, X. Chen, X. Zeng, *J. Alloys Compd.* **2012**, *513*, 518.
[9] P. M., G. K., L. F.B., Euro PM2019 Proc. **2019**.
[10] H. Yang, Y. Zhang, J. Wang, Z. Liu, C. Liu, S. Ji, *J. Mater. Sci. Technol.* **2021**, *91*, 215.
[11] E. Cerri, E. Ghio, *Mater. Sci. Eng.* **2023**, *881*, 145402.
[12] L. E. Murr, S. A. Quinones, S. M. Gaytan, M. I. Lopez, A. Rodela, E. Y. Martinez, D. H. Hernandez, E. Martinez, F. Medina, R. B. Wicker, *J. Mech. Behav. Biomed. Mater.* **2009**, *2*, 20.
[13] C. Li, H. Gu, W. Wang, S. Wang, L. Ren, Z. Wang, Z. Ming, Y. Zhai, *Mater. Technol.* **2020**, *36*, 1516.
[14] S. Spigarelli, C. Paoletti, M. Cabibbo, E. Cerri, E. Santecchia, *Addit. Manuf.* **2021**, *49*, 102520.
[15] Z. Bingjing, W. Hong, Q. Ning, W. Chao, H. Min, *Mater. Sci. Eng.* **2016**, *70*, 832.
[16] J. D. Avila, S. Bose, A. Bandyopadhyay, *Titan. Med. Dent. Appl.* **2018**, 325, https://doi.org/10.1016/B978-0-12-812456-7.00015-9.
[17] A. Basak, S. Das, *J. Alloys Compd.* **2017**, *705*, 806.
[18] W. Hearn, R. Steinlechner, E. Hryha, *Powder Metall.* **2022**, *65*, 121.
[19] J. J. S. Dilip, G. D. J. Ram, T. L. Starr, B. Stucker, *Addit. Manuf.* **2017**, *13*, 49.
[20] X. Li, Y. H. Tan, H. J. Willy, P. Wang, W. Lu, M. Cagirici, C. Y. A. Ong, T. S. Herng, J. Wei, J. Ding, *Mater. Des.* **2019**, *178*, 107881.
[21] R. Seede, D. Shoukr, B. Zhang, A. Whitt, S. Gibbons, P. Flater, A. Elwany, R. Arroyave, I. Karaman, *Acta Mater.* **2020**, *186*, 199.
[22] M. Ramsperger, L. Mujica Roncery, I. Lopez Galilea, R. Singer, W. Theisen, C. Körner, *Adv. Eng. Mater.* **2015**, *47*, 1469.
[23] M. Ramsperger, R. Singer, C. Körner, *Metall. Mater. Trans.* **2016**, *47*, 1469.
[24] L. N. Carter, C. Martin, P. J. Withers, M. M. Attallah, *J. Alloys Compd.* **2014**, *615*, 338.
[25] L. E. Murr, E. Martinez, X. M. Pan, S. M. Gaytan, J. A. Castro, C. A. Terrazas, F. Medina, R. B. Wicker, D. H. Abbott, *Acta Mater.* **2013**, *61*, 4289.
[26] M. H. Haafkens, J. Matthey, *Weld. J.* **1982**, *61*, 25.
[27] A. V. Agapovichev, A. I. Khaimovich, V. G. Smelov, V. V. Kokareva, E. V. Zemlyakov, K. D. Babkin, A. Y. Kovchik, *Materials* **2023**, *16*, 2088.
[28] B. Albert, R. Völkl, U. Glatzel, *Metall. Mater. Trans.* **2014**, *45*, 4561.
[29] Ł. Rakoczy, M. Grudzień-Rakoczy, R. Cygan, T. Kargul, Ł. Maj, A. Zielińska-Lipiec, *Metall. Mater. Trans.* **2023**, *54*, 3630.
[30] F. Geiger, K. Kunze, T. Etter, *Mater. Sci. Eng.* **2016**, *661*, 240.
[31] Y. Hagedorn, J. Risse, W. Meiners, N. Pirch, K. Wissenbach, R. Poprawe, *High Value Manufacturing: Advanced Research In Virtual And Rapid Prototyping, 6th International Conference on Advanced Research in Virtual and Rapid Prototyping, held in Leiria, Portugal*, CRC Press, London **2013**, pp. 291–295.
[32] A. Seidel, T. Finaske, A. Straubel, H. Wendrock, T. Maiwald, M. Riede, E. Lopez, F. Brueckner, C. Leyens, *Metall. Mater. Trans.* **2018**, *49*, 3812.
[33] J. Bracci, K. Kaufmann, J. Schlatter, J. Vecchio, N. Zhou, S. Jiang, K. S. Vecchio, J. Cheney, *Front. Met. Alloys* **2024**, *3*, 1397636.
[34] E. Martin, A. Natarajan, S. Kottilingam, R. Batmaz, *Addit. Manuf.* **2021**, *39*, 101894.
[35] T. Dahmen, N. G. Henriksen, K. V. Dahl, A. Lapina, D. B. Pedersen, J. H. Hattel, T. L. Christiansen, M. A. J. Somers, *Addit. Manuf.* **2021**, *39*, 101912.
[36] H. Y. Bor, C. Hsu, C. N. Wei, *Mater. Chem. Phys.* **2004**, *84*, 284.
[37] G. H. Lee, B. Kim, J. B. Jeon, M. Park, S. Noh, B. J. Kim, *Mater. Sci. Eng. A.* **2025**, *924*, 147776.
[38] M. Bensch, A. Sato, N. Warnken, E. Affeldt, R. C. Reed, U. Glatzel, *Acta Mater.* **2012**, *60*, 1206036.
[39] E. Fleischmann, M. K. Miller, E. Affeldt, U. Glatzel, *Acta Mater.* **2015**, *87*, 1412011.
[40] M. V. Nathal, *Met. Trans. A* **1987**, *18A*, 2647026.
[41] T. Murakumo, T. Kobayashi, Y. Koizumi, H. Harada, *Acta Mater.* **2004**, *52*, 0404028.

